# MAE 545 Final Report

*Aerodynamic Characterization of a Re-Entry Ballistic Capsule*

**Kevin Andrade, Nina Arcot, Nathan Spilker, and Kaley Ubellacker**

Department of Aerospace Engineering
Princeton University
17 March 2022

# 1    Introduction

The objective of the MAE 545 project is to perform the aerothermodynamic characterization of an orbital Re-entry Ballistic Capsule and define its Thermal Protection System (TPS). The geometry under study in this project is a ballistic, blunt-body, sphere-cone vehicle which contains a heat shield that will be stowed in the away position upon launch, and will only be deployed upon reentry. A rendering of this vehicle is shown in Figure 1. The motivation behind the study of this particular geometric configuration is its portability which is especially crucial for the upper stages of launch vehicles. The geometry also has the added benefit of a larger deceleration in the upper atmosphere.
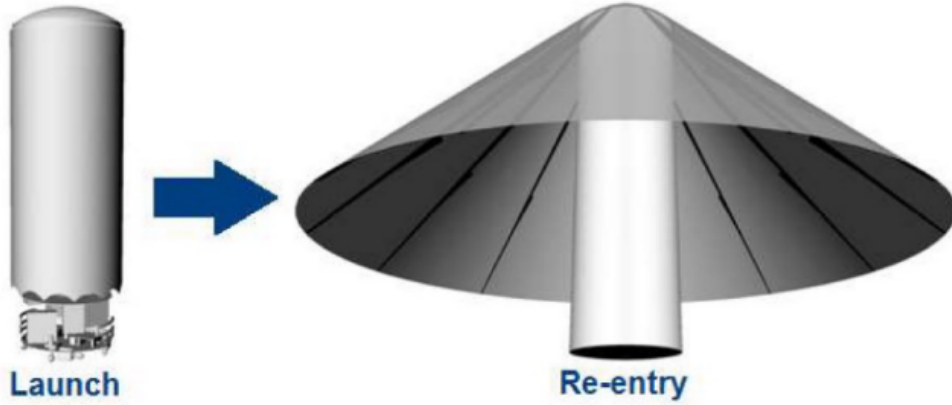


Figure 1: Model of Configuration Under Study

The analysis for the first half of the project was divided into two separate phases. In the first phase, we calculated an initial trajectory and estimation of aerodynamic forces on the vehicle. The methods used to solve this problem analytically an numerically were developed in class and were solved using MATLAB.

# 2    Task 1

Entry path analysis is an important step in the design process, as it returns values of interest as we progress through the design timeline. The relevant values for this analysis include acceleration, time of flight, and dynamic pressure, among others. Assuming zero angle of attack along the trajectory, the equations of motion for a ballistic reentry are defined as follows:

$$\frac{dV}{dz} = -\frac{1}{2}\rho V \frac{1}{\sin(\gamma k_d)} - (\frac{g}{V} - \frac{V}{r})$$

$$\frac{d\gamma}{dz} = -(\frac{g}{V^2} - \frac{1}{r})\frac{1}{\tan\gamma}$$

## 2.1    Velocity Profile

The equations of motion were solved both analytically and numerically to develop the velocity profile, as shown in Figure 2. For both the numerical and the analytical solutions, it was assumed that the ballistic coefficient was constant; this comparison was done for an initial entry angle of $\gamma = -1.13°$ and a constant drag coefficient of $C_d = 0.8$. The analytical solution assumed that flight path angle was constant to obtain a closed form solution. Another key difference between the two solutions were their density models: the analytical solution assumed an exponential density model whereas the numerical solution used the 1976 Standard Atmosphere Model. For the numerical solution, Euler's Forward method was solved in MATLAB starting from the initial re-entry height. The iterations for this were conducted according to the following formulas for velocity and flight path angle:

$$V_{n+1} = V_n + \frac{1}{2}\rho_n V_n \frac{1}{\sin(\gamma_n k_d)} + (\frac{g_{n+1}}{V_n} - \frac{V_n}{r_{n+1}})\Delta H$$

$$\gamma_{n+1} = \gamma_n + (\frac{g_{n+1}}{V_n^2} - \frac{1}{r_{n+1}})\frac{1}{\tan\gamma_n}\Delta H$$

In the above Euler's method, n is the running iteration index and H is the height, such that

$$\Delta H = H_{n+1} - H_n$$

is the altitude step size.

It can be seen that the numerical solution greatly differs from the analytical solution due to assumptions related to density and the flight path angle. It is also clear that much of the deceleration occurs in a specific range of altitudes during the descent, which will impact the mechanical and thermal loads on the vehicle. Using the numerical solution, it is also possible to gain a preliminary understanding of how the capsule configuration will impact the trajectory. Figures 3 and 4 show how the velocity and flight path angle change throughout the descent depending on the drag coefficient, $C_d$. Specifically, higher $C_d$ leads to a sharp decrease in velocity and $\gamma$ occurring at higher altitudes. This is important since the velocity at different altitudes will determine the maximum dynamic pressure, and the flight path angle will impact the pressure coefficient distribution.
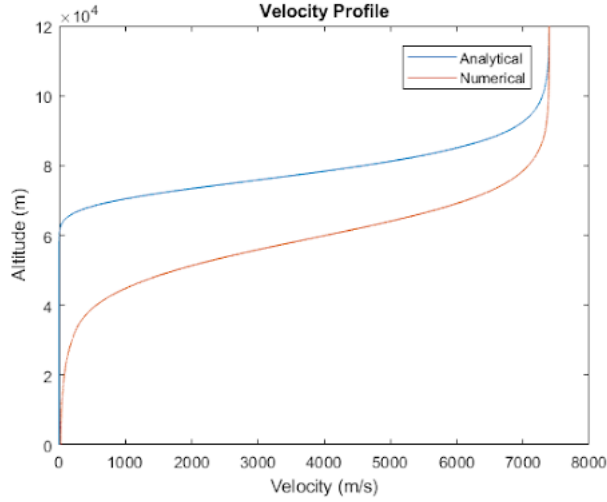


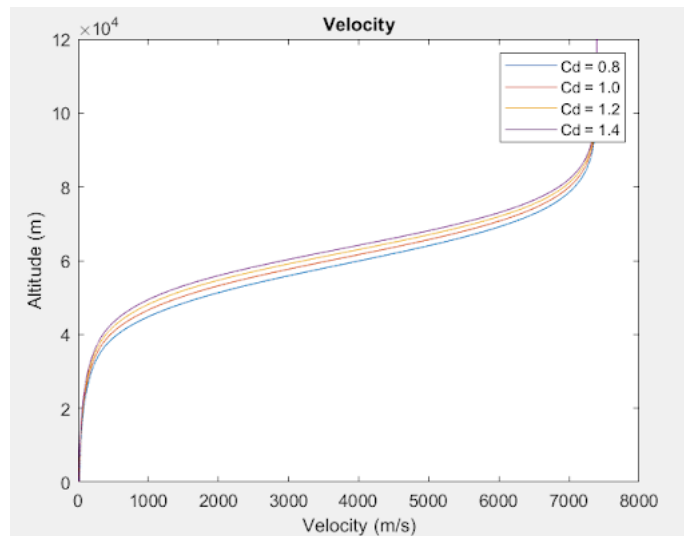Figure 2: Velocity profiles resulting from both analytical and numerical methods



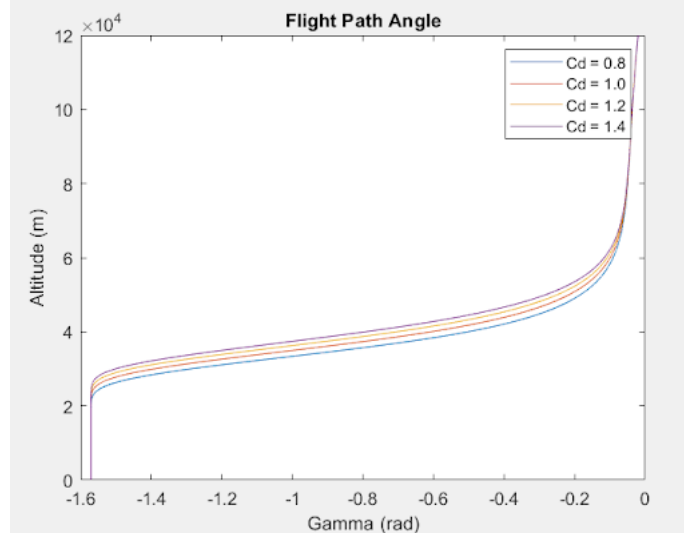Figure 3: Velocity profiles solved numerically with different $C_d$ values

Figure 4: Variation in flight path angle, $\gamma$, for different $C_d$ values

## 2.2 Preliminary Flight Scenario

After generating the velocity profile, several flight parameters, including dynamic pressure $(q)$, Mach number $(M)$, acceleration $(a)$, and Reynolds Number $(Re)$, were calculated using the following equations:

$$q = \frac{1}{2}\rho V^2$$

$$M = \frac{V}{\sqrt{\gamma RT}}$$

$$a = \frac{dV}{dt}$$

$$Re = \frac{\rho V S}{\mu}$$

Note that $\rho$ is density, $V$ is velocity, $\gamma$ is the specific heat ratio (assumed to be 1.4 for air), $R$ is the gas constant for air, $T$ is temperature, $S$ is a reference area, and $\mu$ is dynamic viscosity. For calculating Reynolds number, the reference area used was the overall, largest diameter of the re-entry capsule. The dynamic viscosity of air depends on temperature and thereby altitude according to the following relation:

$$\mu = \frac{\beta T^{\frac{3}{2}}}{T + S}$$

In the above equation, $\beta$ and S are non-dimensional constants, where $\beta$ equals $1.458 \times 10^{-6}$, and S equals 110.4. Note, this is a different $S$ and is not the same as reference area. Figure 5 shows that increasing the drag coefficient leads to reduced dynamic pressure, whereas Figure 6 shows that increasing $C_d$ results in higher Mach number.
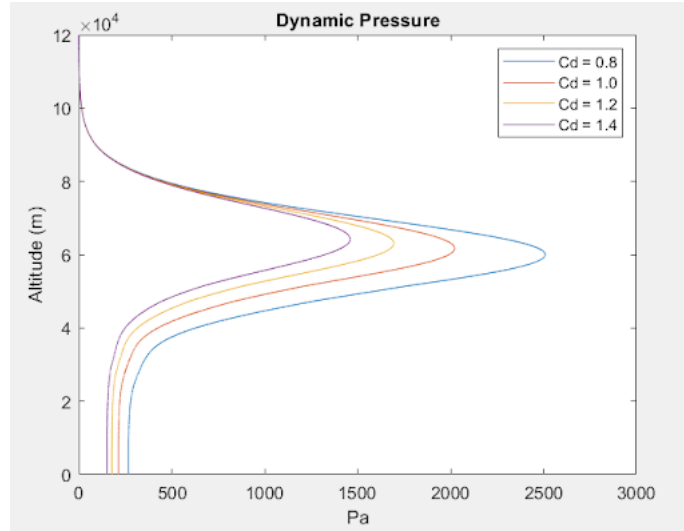
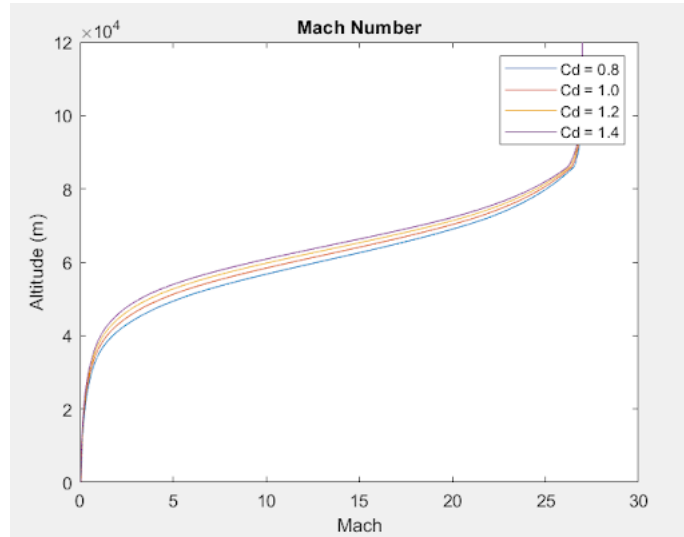Figure 5: Dynamic pressure for different $C_d$ values



Figure 6: Variation in Mach number for different $C_d$ values

Figures 7 and 8 show how acceleration changes throughout the descent and indicate that higher $C_d$ leads to a slightly higher maximum g-loading. Lastly, Figure 9 shows that larger $C_d$ corresponds to lower Reynolds number, and in both cases, the Reynolds number is higher at lower altitudes, indicating a transition from laminar to turbulent flow during the descent.
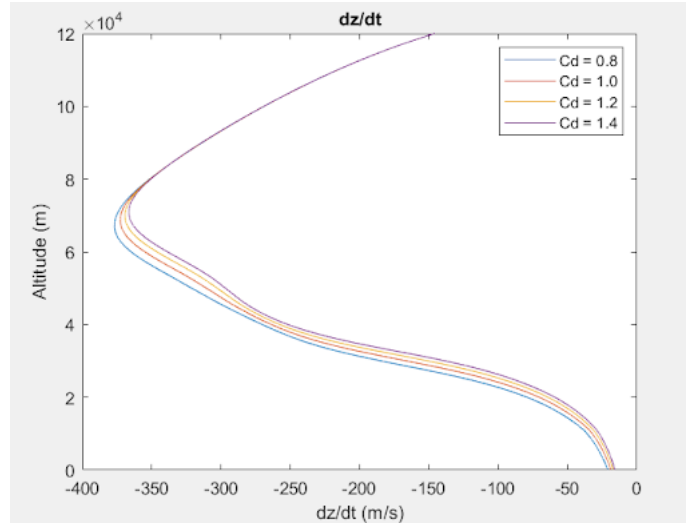
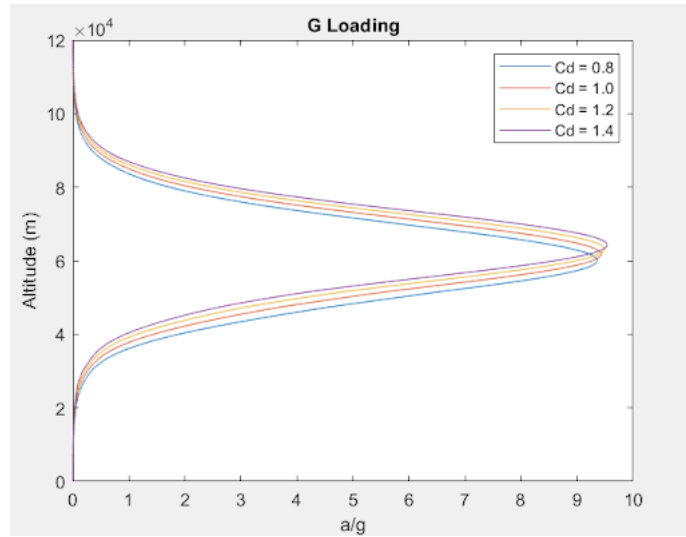Figure 7: Acceleration profile for different $C_d$ values



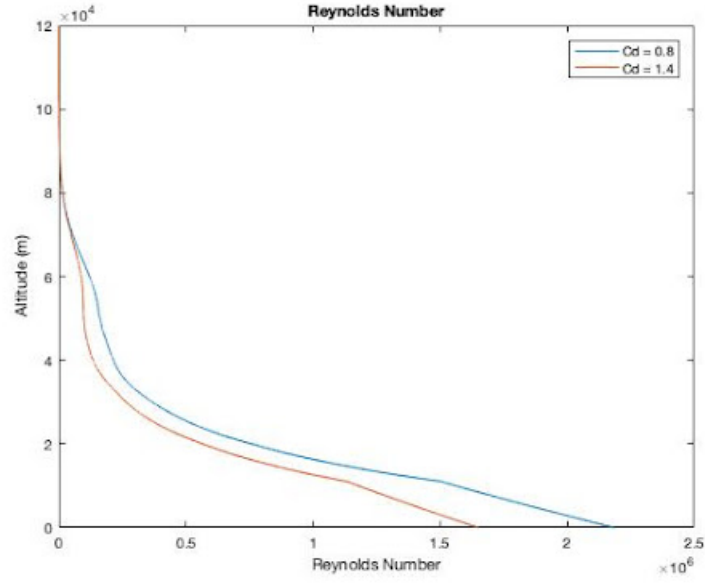Figure 8: G loads for different $C_d$ values

Figure 9: Reynolds number for different $C_d$ values

After determining the preliminary flight scenario, the time of flight was calculated for different values of $C_d$ and a test matrix was generated for use in Task 2. These results are shown in Figures 10 and 11.

| | Cd = 0.8 | Cd = 1.0 | Cd = 1.2 | Cd = 1.4 |
|---|---|---|---|---|
| Time of flight (seconds) | 974 | 1060 | 1130 | 1200 |

Figure 10: Time of flight for different $C_d$ values

| Velocity (m/s) | Static Temp. (K) | Density (kg/m3) | Mach Number | Gamma (deg) | Height (m) |
|---|---|---|---|---|---|
| 7.3966e+03 | 360 | 2.2226e-08 | 26.9851 | -1.1300 | 120000 |
| 7.3958e+03 | 239.9997 | 9.6920e-08 | 26.9820 | -1.6733 | 110000 |
| 7.3869e+03 | 195.0813 | 5.5942e-07 | 26.9497 | -2.0868 | 100000 |
| 7.3357e+03 | 186.8673 | 3.4102e-06 | 26.7625 | -2.4507 | 90000 |
| 7.0808e+03 | 198.6558 | 1.8456e-05 | 25.0574 | -2.8455 | 80000 |
| 6.1397e+03 | 219.5991 | 8.2822e-05 | 20.6610 | -3.5058 | 70000 |
| 4.0259e+03 | 247.0643 | 3.0962e-04 | 12.7678 | -5.2008 | 60000 |
| 1.7595e+03 | 270.6500 | 0.0010 | 5.3296 | -10.5201 | 50000 |
| 561.0246 | 250.3247 | 0.0040 | 1.7668 | -28.8037 | 40000 |
| 192.2692 | 226.5057 | 0.0184 | 0.6367 | -73.7800 | 30000 |
| 79.2204 | 216.6500 | 0.0889 | 0.2683 | -89.9898 | 20000 |
| 35.9846 | 223.2625 | 0.4135 | 0.1200 | -90.0000 | 10000 |
| 20.8790 | 288.1500 | 1.2250 | 0 | -90.0000 | 0 |

Figure 11: Test matrix summarizing Task 1 outcomes

# 3 Task 2

The second task was centered around the aerodynamic analysis of the vehicle. Using approximate methods, we were able to analyze the pressure distribution around the vehicle at various angles of attack. Calculating the pressure distribution was important for calculating aerodynamic forces, since the highest contributor to aerodynamic forces are the pressure forces (for this specific problem), as was shown in class. This lead directly into the calculation of lift, drag, normal, axial, and moment coefficients through consideration of their contributions to each direction.

## 3.1 Pressure Coefficients

The initial phase of Task 2 required the calculation of the pressure coefficient acting around the vehicle for various angles of attack which would then be used to analyze both the pressure loads and aerodynamic coefficients. This analysis for $C_p$ was calculated differently for the base and the windward side since their location implies a different pressure coefficient approximation. For the base of the vehicle, the pressure coefficient was calculated using the approximation for reentry vehicles with a large base area at high Mach numbers and angles of attack which is given by the following relationship:

$$C_{p,base} \approx -\frac{2}{\gamma M_\infty^2} \tag{1}$$

The pressure coefficient for the windward side of the vehicle was then calculated using the Modified Newtonian Method for a standing normal shock acting on blunt bodies given by:

$$C_{p,windward} = C_{p,0} \frac{\sin^2(\theta)}{\sin^2(\theta_0)} = \frac{2}{\gamma M_1^2}(\frac{p_{2,0}}{p_1} - 1)\frac{\sin^2(\theta)}{\sin^2(\theta_0)} \tag{2}$$

Based on the 45 deg angle on the conical section of the vehicle, we were able to assume that flow remained subsonic on the windward side of the vehicle. This allowed us to use Newtonian theory which was applied for calculation of all windward coefficients of pressure. The angle $\theta$ was calculated using the normal vectors for each of the various faces that make up the STL file of the vehicle. After the normal vectors and vertices were extracted from the geometry file using the given MATLAB file, the theta was found as the dot product of the face's normal vector and the normalized velocity. This allowed us to calculate the pressure coefficient for the vehicle at each of its faces. Below, we have shown some pressure distributions at various angles of attack and Mach numbers(Figures 12 - 14):
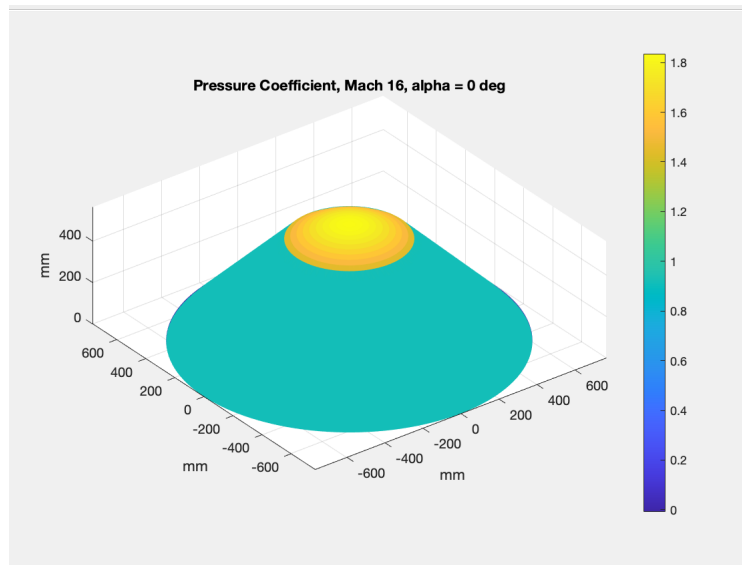


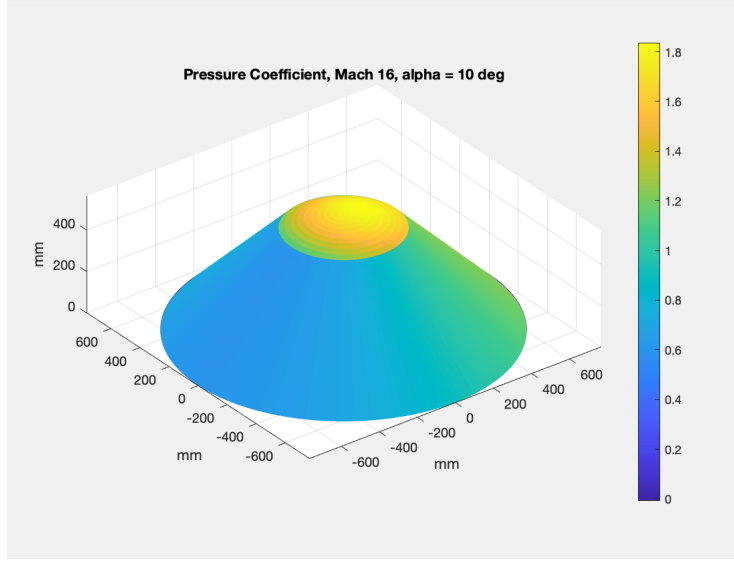Figure 12: Pressure Coefficient Distribution for Mach 16 at 0 AOA

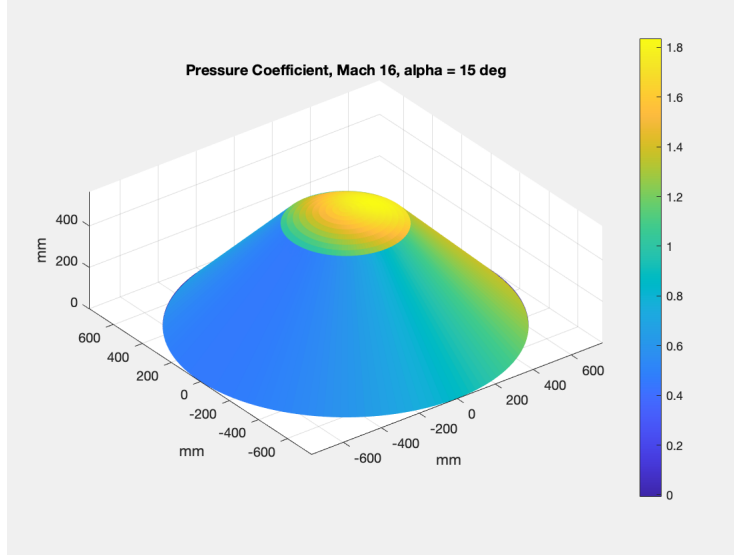Figure 13: Pressure Coefficient Distribution for Mach 16 at 10 AOA



Figure 14: Pressure Coefficient Distribution for Mach 16 at 15 AOA

## 3.2   Aerodynamic Coefficients

In order to accurately calculate the aerodynamic coefficients, we found that we needed to remove half of the mesh points since some of the read-in code caused a doubling of points that was initially causing our coefficients to be off by a factor of two. After filtering through these mesh points appropriately, we began the analysis by calculating the normal forces, axial forces, and moment coefficients acting on the vehicle. These were calculated by considering the the pressure force contribution in each direction summed over each of the cells within the adjusted mesh.

$$f_A \approx \sum_{j=1}^{F} (-p_j) n_{z,j} \Delta S_j = A_p \tag{3}$$

$$f_N \approx \sum_{j=1}^{F} (-p_j) n_{x,j} \Delta S_j = N_p \tag{4}$$

$$M_y \approx \sum_{j=1}^{F} [-(x_j - x_{cg})(-p_j)n_{x,j} + (z_j - z_{cg})(-p_j)n_{x,j}]\Delta S_j \tag{5}$$

The normal and axial coefficients were then calculated using the equations below where $S_{ref}$ was considered to be the largest area which in this case is the base area of the vehicle.

$$C_A = \frac{A}{0.5\rho V_\infty^2 S_{ref}} \tag{6}$$

$$C_N = \frac{N}{0.5\rho V_\infty^2 S_{ref}} \tag{7}$$

With the calculation of the normal and axial coefficients, we then did a projection of the each coefficient onto the X and -Z axes with the additional consideration of the angle of attack $\alpha$. This results in the following equations for lift and drag coefficients:

$$C_{L,p} = C_{N,p}\cos(\alpha) - C_{A,p}\sin(\alpha) \tag{8}$$

$$C_{D,p} = C_{N,p}\sin(\alpha) + C_{A,p}\cos(\alpha) \tag{9}$$

Then in order to calculate the overall lift and drag coefficients, the coefficients were summed over each of the adjusted number of faces $F$ over the vehicle which approiximates taking the integral over the geometry. The results plotted below (Figures 15, 16, 17) which show each coefficient vs. Mach number at various angles of attack.
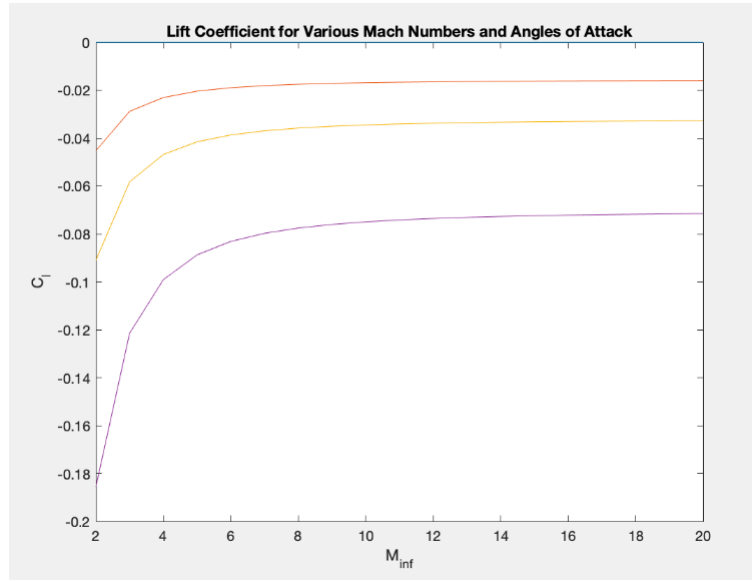


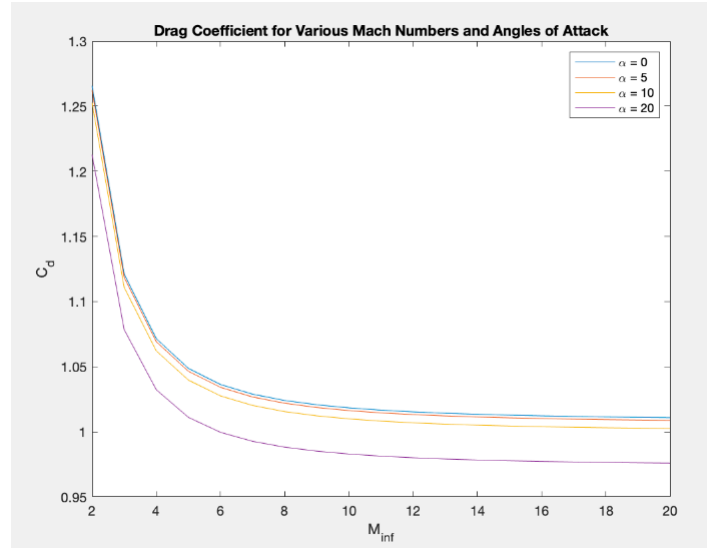Figure 15: Lift Coefficient for Various Mach Numbers and Angles of Attack

Figure 16: Drag Coefficient for Various Mach Numbers and Angles of Attack
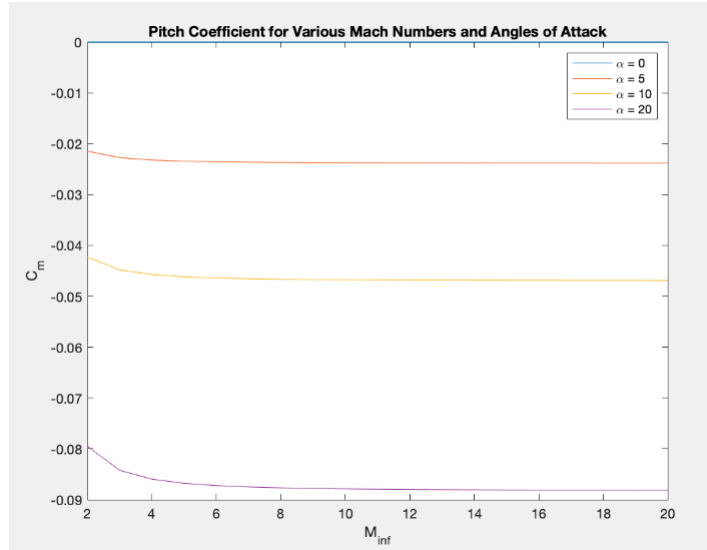


Figure 17: Moment Coefficient for Various Mach Numbers and Angles of Attack

An aerodynamic database was also generated in order to calculate the optimal trajectory with the updated aerodynamic analysis. Given the exclusive dependency of the coefficients on angle of attack $\alpha$ and Mach number $M$, the database which is show below (Figure 18) contains only values of varying $M$ and $\alpha$ with the corresponding $C_L$, $C_D$, $C_M$.

| Mach # | Angle of Attack (deg) | C_L | C_D | C_M |
|---|---|---|---|---|
| 2 | 0 | 0 | 1.2656 | 0 |
| 2 | 5 | -0.0452 | 1.2624 | -0.0215 |
| 2 | 10 | -0.091 | 1.2527 | -0.0423 |
| 2 | 20 | -0.1855 | 1.2127 | -0.0795 |
| 3 | 0 | 0 | 1.1212 | 0 |
| 3 | 5 | -0.0288 | 1.1186 | -0.0228 |
| 3 | 10 | -0.0582 | 1.1109 | -0.0448 |
| 3 | 20 | -0.1214 | 1.0784 | -0.0842 |
| 4 | 0 | 0 | 1.0715 | 0 |
| 4 | 5 | -0.023 | 1.0692 | -0.0232 |
| 4 | 10 | -0.0468 | 1.0621 | -0.0457 |
| 4 | 20 | -0.0991 | 1.0323 | -0.086 |
| 5 | 0 | 0 | 1.0487 | 0 |
| 5 | 5 | -0.0204 | 1.0465 | -0.0234 |
| 5 | 10 | -0.0415 | 1.0397 | -0.0462 |
| 5 | 20 | -0.0887 | 1.0111 | -0.0868 |
| 6 | 0 | 0 | 1.0363 | 0 |
| 6 | 5 | -0.0189 | 1.0342 | -0.0236 |
| 6 | 10 | -0.0387 | 1.0276 | -0.0464 |
| 6 | 20 | -0.0831 | 0.9996 | -0.0872 |
| 7 | 0 | 0 | 1.0289 | 0 |
| 7 | 5 | -0.0181 | 1.0268 | -0.0236 |
| 7 | 10 | -0.0369 | 1.0203 | -0.0466 |
| 7 | 20 | -0.0797 | 0.9927 | -0.0875 |
| 8 | 0 | 0 | 1.0241 | 0 |
| 8 | 5 | -0.0175 | 1.022 | -0.0237 |
| 8 | 10 | -0.0358 | 1.0155 | -0.0466 |
| 8 | 20 | -0.0775 | 0.9882 | -0.0877 |
| 9 | 0 | 0 | 1.0208 | 0 |
| 9 | 5 | -0.0171 | 1.0187 | -0.0237 |
| 9 | 10 | -0.035 | 1.0123 | -0.0467 |
| 9 | 20 | -0.076 | 0.9852 | -0.0878 |
| 10 | 0 | 0 | 1.0184 | 0 |
| 10 | 5 | -0.0168 | 1.0163 | -0.0237 |
| 10 | 10 | -0.0345 | 1.01 | -0.0468 |
| 10 | 20 | -0.0749 | 0.983 | -0.0879 |
| 11 | 0 | 0 | 1.0167 | 0 |
| 11 | 5 | -0.0166 | 1.0146 | -0.0238 |
| 11 | 10 | -0.0341 | 1.0082 | -0.0468 |
| 11 | 20 | -0.0742 | 0.9813 | -0.0879 |
| 12 | 0 | 0 | 1.0153 | 0 |
| 12 | 5 | -0.0165 | 1.0133 | -0.0238 |
| 12 | 10 | -0.0338 | 1.0069 | -0.0468 |
| 12 | 20 | -0.0735 | 0.9801 | -0.088 |
| 13 | 0 | 0 | 1.0143 | 0 |
| 13 | 5 | -0.0164 | 1.0122 | -0.0238 |
| 13 | 10 | -0.0335 | 1.0059 | -0.0468 |
| 13 | 20 | -0.0731 | 0.9791 | -0.088 |
| 14 | 0 | 0 | 1.0135 | 0 |
| 14 | 5 | -0.0163 | 1.0114 | -0.0238 |
| 14 | 10 | -0.0333 | 1.0051 | -0.0469 |
| 14 | 20 | -0.0727 | 0.9784 | -0.088 |
| 15 | 0 | 0 | 1.0128 | 0 |
| 15 | 5 | -0.0162 | 1.0108 | -0.0238 |
| 15 | 10 | -0.0332 | 1.0045 | -0.0469 |
| 15 | 20 | -0.0724 | 0.9778 | -0.0881 |
| 16 | 0 | 0 | 1.0123 | 0 |
| 16 | 5 | -0.0161 | 1.0102 | -0.0238 |
| 16 | 10 | -0.0331 | 1.0039 | -0.0469 |
| 16 | 20 | -0.0722 | 0.9773 | -0.0881 |
| 17 | 0 | 0 | 1.0118 | 0 |
| 17 | 5 | -0.0161 | 1.0098 | -0.0238 |
| 17 | 10 | -0.033 | 1.0035 | -0.0469 |
| 17 | 20 | -0.0719 | 0.9768 | -0.0881 |
| 18 | 0 | 0 | 1.0115 | 0 |
| 18 | 5 | -0.016 | 1.0094 | -0.0238 |
| 18 | 10 | -0.0329 | 1.0031 | -0.0469 |
| 18 | 20 | -0.0718 | 0.9765 | -0.0881 |
| 19 | 0 | 0 | 1.0111 | 0 |
| 19 | 5 | -0.016 | 1.0091 | -0.0238 |
| 19 | 10 | -0.0328 | 1.0028 | -0.0469 |
| 19 | 20 | -0.0716 | 0.9762 | -0.0881 |
| 20 | 0 | 0 | 1.0109 | 0 |
| 20 | 5 | -0.016 | 1.0088 | -0.0238 |
| 20 | 10 | -0.0327 | 1.0025 | -0.0469 |
| 20 | 20 | -0.0715 | 0.976 | -0.0881 |

Figure 18: Aerodynamic Database

Now that we have updated values of our aerodynamic coefficients, we can improve our assumption of constant ballistic coefficient for the numerical trajectory solution in task 1. Calculating an improved value of the ballistic coefficient along the trajectory, we find the plots shown in Figures 19, 20, and 21, again for our initial condition of $h = 120km$ and $\gamma = -1.13$.
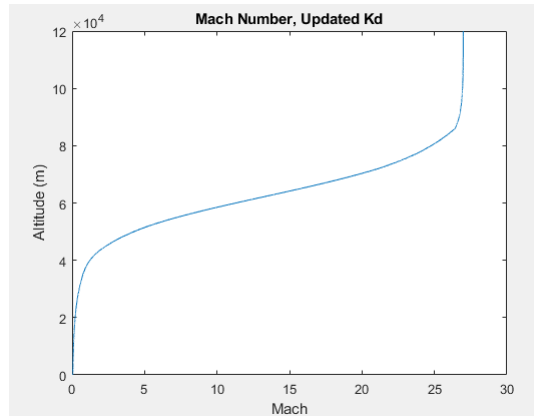

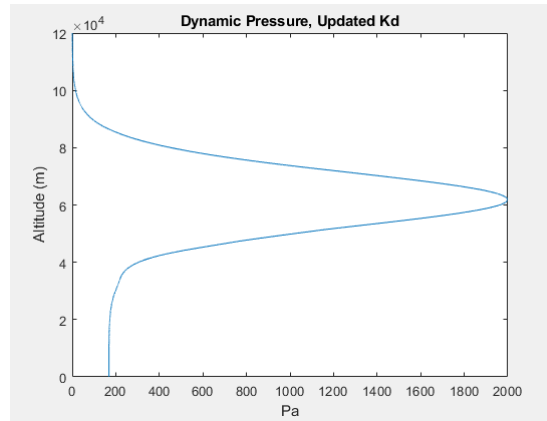
Figure 19: Height versus Mach number, updated aerodynamics

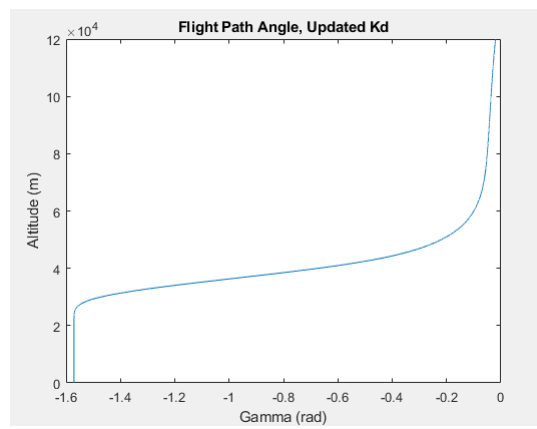Figure 20: Height versus dynamic pressure, updated aerodynamics



Figure 21: Height versus flight path angle, updated aerodynamics

# 4 Task 3

The objective of the third task was to determine the aerothermodynamic and intertial loads on the ballistic re-entry capsule along an optimized flight trajectory. The completion of this task was accomplished by dividing analysis into three sections around the capsule, including the stagnation point, spherical nose cap, and conical section. Different correlations were applied to each of these sections to determine the heat flux at every point on the capsule. Body surface temperature was determined accounting for re-radiated heat as altitude varies. This provided an adequate basis with which to understand the thermal loads the capsule is subjected to along its trajectory and conduct further analysis in the final task to define the thermal protection system.

## 4.1 Flight Conditions

### 4.1.1 Optimized Trajectory

The optimized flight trajectory for the re-entry capsule was provided as part of the project's given material. Figure 22 below displays the discretized optimized trajectory.
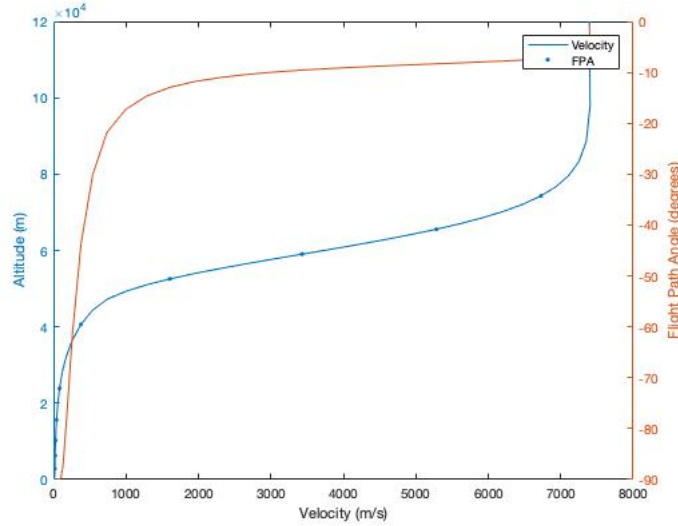


Figure 22: Optimized flight trajectory with velocity and flight path angle (FPA) for 10 discretized points.

It can be observed that the capsule experiences the greatest deceleration between about 40 km and 80 km. This provides a sufficient basis of understanding for where we can expect the highest thermal loads. This finding is supplemented in Figure 23 with a plot of the capsule's deceleration along its trajectory. It can be observed that the capsule experiences a maximum deceleration magnitude of approximately 195 meters per second squared, and this occurs at an altitude of approximately 63 kilometers.

### 4.1.2 Flow around the Capsule

Along its reentry path, the atmospheric conditions surrounding the capsule can be divided into three primary sections, as shown below in Figure 24. The adiabatic entry conditions at each section were determined by considering the underlying physical phenomenon. For points along the capsule's flight trajectory where the flow is supersonic, there is a normal shock in front of the stagnation point that compresses the entry flow. The following relations were used to calculate the entry flow conditions, located at point 2 in Figure 24:

$$p_2 = [1 + \frac{2\gamma}{\gamma + 1}(M_1^2 - 1)]p_1 \tag{10}$$

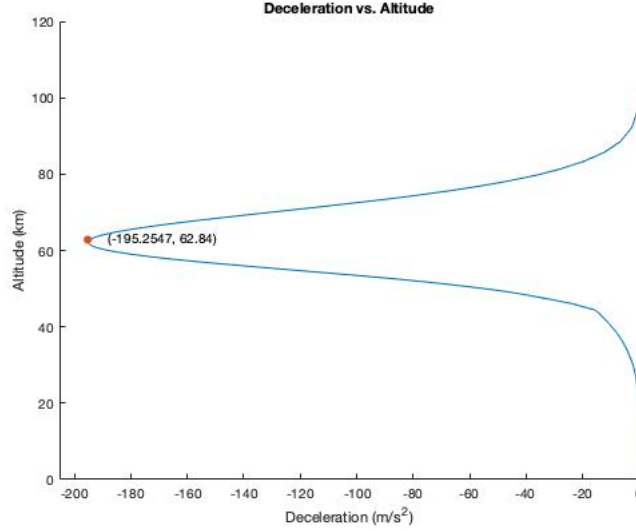$$\rho_2 = [\frac{(\gamma + 1)M_1^2}{2 + (\gamma - 1)M_1^2}]\rho_1 \tag{11}$$

Figure 23: Plot of deceleration expressed as a function of altitude along the optimized trajectory.

$$T_2 = \frac{[2\gamma M_1^2 - (\gamma - 1)][(\gamma - 1)M_1^2 + 2]}{(\gamma + 1)^2 M_1^2} \tag{12}$$

where $p$ is pressure, $\gamma$ is the specific heat ratio, $M$ is Mach number, $\rho$ is density, and subscripts represent the corresponding flow section.

The flow conditions determined at section 2 were used to calculate the stagnation point heat flux. The flow surrounding the nose cone was assumed to have the same properties as section 2. For the flow around the conical section, the relevant properties were calculated using oblique shock relations, similar to the normal shock relations. To find the normal component of the flow, the theta-beta-mach relations were used with the weak shock solution and a 45°cone angle. It was assumed that the flow conditions entering the oblique shock were atmospheric.
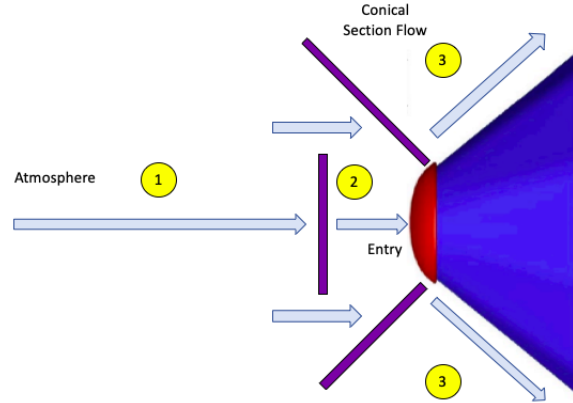


Figure 24: Flow conditions surrounding the capsule during supersonic flight according to the following sections: 1) atmospheric flow before a normal shock, 2) flow for entry conditions after the normal shock in front of the stagnation point, and 3) flow after turning due to an oblique shock at the beginning of the conical section. Arrows denote the flow, and the purple lines denote shocks.

### 4.1.3 Radiative Heating

Radiative heating was updated at each point along the trajectory for calculations. This was accomplished using a combination of the Stefan-Boltzmann law with the Tauber-Menees method, as described by the

equation below:

$$q^R_{wall} = \epsilon \sigma T_w^{0.25} \tag{13}$$

where $\epsilon$ is emissivity, and $\sigma$ is the Stefan-Boltzmann constant and is equal to $5.6695 \times 10^{-8}$. Using the above relation for re-radiated heating and assuming incident heating is balanced by the re-rediated heat, the following relation allowed us to update the surface temperature at each point in time along the capsule's flight path:

$$\epsilon \sigma T_w^{0.25} + B_q T_w = A_q \tag{14}$$

where the parameters $A_q$ and $B_q$ were defined as follows:

$$A_q = 1.83 \times 10^{-4} R_N^{-0.5} \rho_\infty^{0.5} V_\infty^3, B_q = \frac{A_q c_p}{H_{aw}};$$

where it is worthwhile to note that $A_q - B_q T_w$ is equal to the convective heating according to the Tauber-Menees method. This produced the following results for surface temperature along the capsule's trajectory, shown in Figure 25. This plot clearly shows that the stagnation point experiences higher incident heating than the conical section, as expected from our physical understanding of the system.
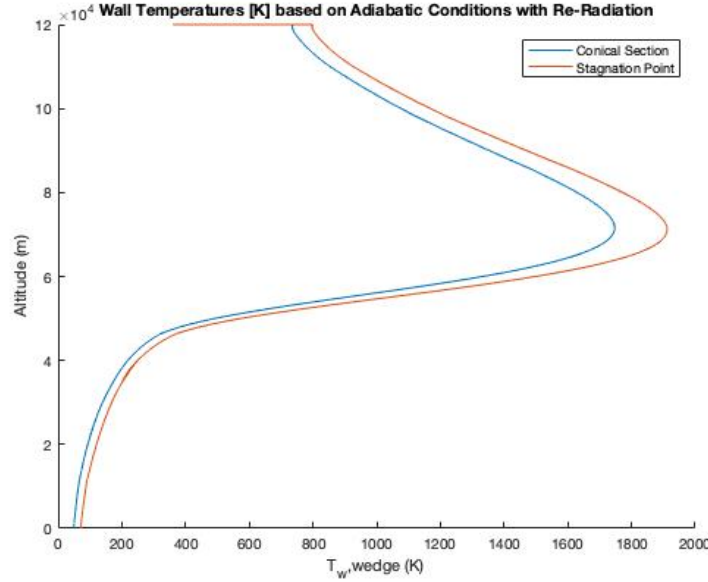


Figure 25: Surface Temperature as a function of altitude in the adiabatic case and accounting for re-radiated heat.

## 4.2 Heat Flux Analysis

A combination of Fay-Riddell, Tauber-Menees and experimental correlations was used to calculate heat flux for the three regions on the capsule. The methods used for each are described further below.

### 4.2.1 Stagnation Point

Both the Fay-Riddell and Tauber-Menees methods were initially used to find heat flux at the stagnation point. The Fay-Ridell stagnation heating correlation was combined with Newtonian theory and used according to the following equation:

$$q_{w,stag} = A \times Pr^{-0.6}(\rho_0 \mu_0)^{0.5} \sqrt{\frac{1}{R_N}}(\frac{2(p_0 - p_\infty)}{\rho_0})^{0.25}(h_{tot} - h_w) \tag{15}$$

where $p_0$, $\rho_0$, and $T_0$ are stagnation values; $h_t ot$ is the total enthalpy and equal to enthalpy for adiabatic conditions at the wall; $h_w$ is enthalpy at the wall; A is set to 0.763 for the spherical geometry; $\mu$ is the dynamic viscosity; $Pr$ is the Prandtl number; and $R_N$ is the radius of the nose. Fay-Riddell accounts for chemistry effects, so it likely gives the better estimate of heat flux conditions at the stagnation point.

For the purpose of comparing values and obtaining a more conservative estimate of the stagnation point heat flux, we also calculated the heat flux using the Tauber-Menees method. This employs the following equation:

$$q_{w,stag} = C\rho_\infty^N V_\infty^M \tag{16}$$

where N = 0.5, M = 3, the $\infty$ subscripts refer to atmospheric conditions, and C is defined by the following:

$$C = (1.83 \times 10^{-8})R_N^{-0.5}(1 - \frac{h_w}{h_{tot}}) \tag{17}$$

For both of the above calculations, re-radiated heat was factored into finding enthalpy at the wall. The results for Fay-Riddell and Tauber-Menees heat flux at the stagnation point are displayed below in Figure 26. Generally speaking, the curves have the same shapes and similar values, until disparities increase near maximum heat flux. It can be observed that the maximum heat flux for Tauber-Menees corresponds to a value of approximately $6.8 \times 10^5$ watts per meter squared, while the maximum heat flux for Fay-Riddell corresponds to a value of approximately $5.5 \times 10^5$ watts per meter squared. These maximum heat fluxes both occur at the same altitude of about 71.2 kilometers. It makes sense that Fay-Riddell has smaller magnitudes of heatflux, especially at the maximum, as compared to Tauber-Menees because Fay-Riddell factors in local conditions past the normal shock in front of stagnation, and Tauber-Menees only factors in external flow properties in the atmosphere. Additionally, this value for maximum heat flux is relatively high. However, that is expected because the stagnation point experiences the highest thermal loads of all locations on the capsule. Moving forward with comparisons on the other two regions, we chose to use Tauber-Menees as a conservative estimate to thermal loads.
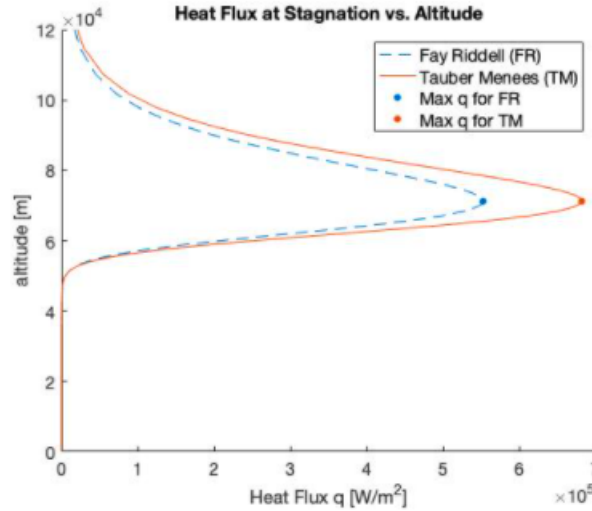


Figure 26: Comparison of the stagnation point's heat flux along the trajectory for both Fay-Riddell and Tauber-Menees correlations.

### 4.2.2   Spherical Nose Cap

For heat flux around the spherical nose cap, the DLR experimental correlation was used. The DLR experimental correlation was well-established from curve-fitting heat transfer distributions, and it uses the heat flux at the stagnation point to make conclusions on the surrounding nose cap, thus providing excellent matching between the stagnation point and the rest of the nose cap. The experimental correlation is represented by the following equation:

$$\frac{q_w(\phi)}{q_{w,stag}} = a\cos^{\frac{3}{2}}(\phi) + b \tag{18}$$

where $\phi$ is the angle from the horizontal to each point along the nose cap, and a and b are experimentally determined coefficients. For DLR, a is equal to 0.855, and b is equal to 0.145. The results of this heat flux analysis along the nose cap is shown below in Figure 27. It can be observed that the heat flux is

highest at the stagnation points and then gradually drops further along the nose cap, approaching the conical section.
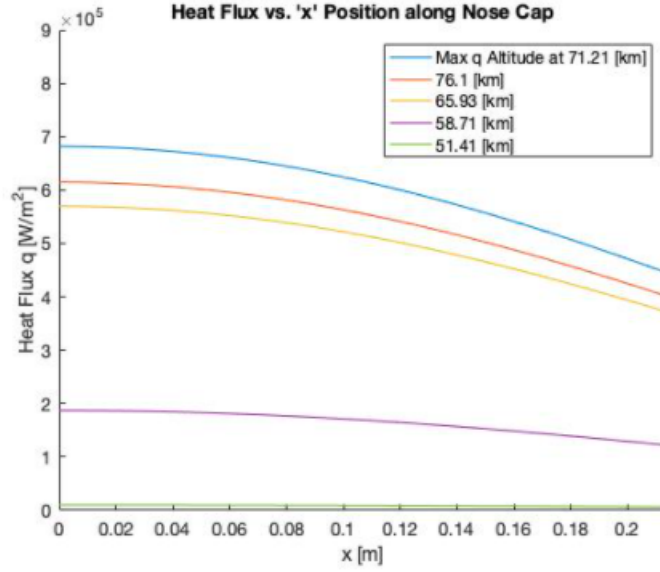


Figure 27: Heat flux on the nose cap for selected altitudes along the capsule's trajectory, where x equals 0 meters corresponds to the stagnation point.

### 4.2.3 Conical Section

The Tauber-Menees method was used once again to calculate heat flux along the conical section. The method differed slightly for the conical section in comparison to the stagnation point, whereby the parameters for the Tauber-Menees relation in Equation 16 change to the following:

$$N = 0.5, M = 3.2, C = 4.03 \times 10^{-5} \cos^{\frac{1}{2}} \alpha \sin \alpha x^{-\frac{1}{2}} (1 - \frac{h_w}{h_{aw}}) \tag{19}$$

where $\alpha$ is the angle of the flow relative to the wall surface, and x is the distance along the section relative to the stagnation point. Figure 28 shows the results for heat flux on the conical section. A similar observation to the nose cap can be made in that the high heat fluxes on the conical section are observed at the very beginning, and for positions farther along the cone, the heat flux decreases and gradually plateaus.

### 4.2.4 Matching

Because Tauber-Menees uses free-stream values to determine heat flux, while the DLR experimental correlation relies on fitted-curves and experimentally evaluated parameters, it is important to analyze how well each of these data sets match, especially at the crossover point from the end of the nose cap to the beginning of the conical section. A plot comparing the nose cap and conical section heat fluxes is shown in Figure 29. There is generally good alignment between the boundary conditions of heat flux at the end of the nose cap and heat flux at the beginning of the conical section. However, this matching could be further improved by using the heat flux at the end of the nose cap as an input condition for calculating the heat flux along the conical section.

## 5  Task 4

The final task was to define the thermal protection system (TPS) required to maintain acceptable temperatures given the calculated aerothermodynamic loads. This was driven by temperature and mass requirements of the capsule, and numerical solutions of the heat equation allowed us to approximate the TPS mass with different constraints and layering strategies. For the purpose of this project, the
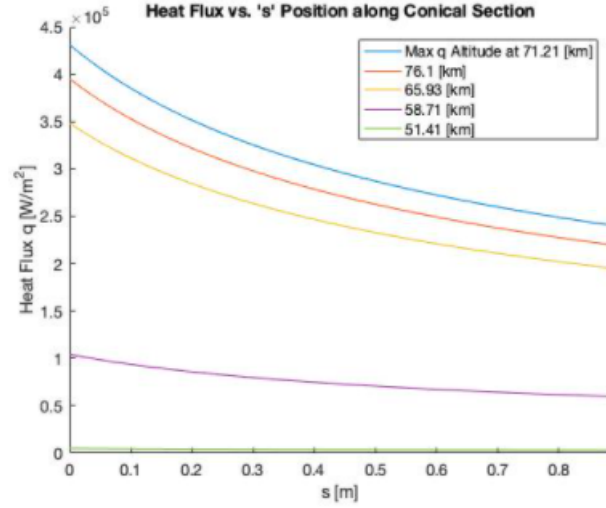
Figure 28: Heat flux on the conical section for selected altitudes along the capsule's trajectory, where s equals 0 meters corresponds to the beginning of the conical section.
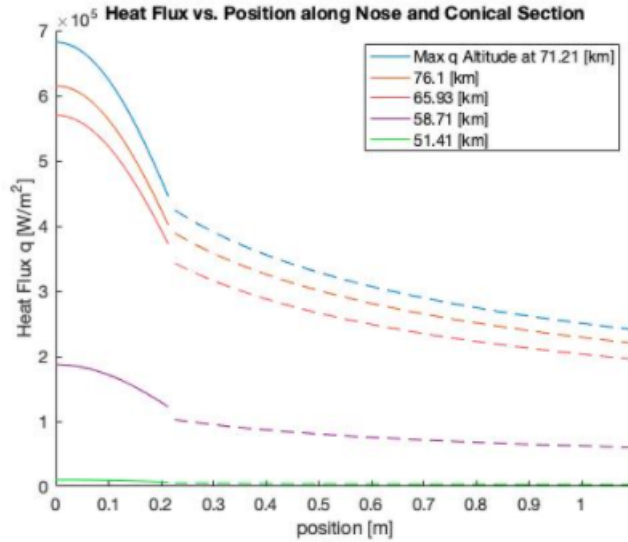


Figure 29: Superimposed results for heat fluxes along both the nose cap and conical section to compare the matching points and alignment of boundary conditions.

analysis was done for the stagnation point, which is the center of the spherical nose cap, as well as at the midpoint of the conical section.

## 5.1 TPS Requirements

### 5.1.1 Thermal Requirements

The primary thermal requirement is that the payload inside of the capsule cannot experience temperatures above 70°C, or 343 K. Thus, the back face temperature of the TPS must be 70°C or less throughout the entire trajectory. Note that the 1976 Standard Atmosphere gives a temperature of around 360 K at the entry altitude of 120 km, but an initial temperature of 343 K was used instead to meet the 70°C requirement. In addition, all of the TPS materials must stay below their maximum operating temperature, which is the highest temperature at which they retain their material properties. This requirement proved easier to meet than the back face temperature.

### 5.1.2 Material Requirements

Given the configuration of the capsule, the TPS materials on the nose cap must be rigid, and the materials on the conical aeroshell must be flexible. Furthermore, the first and last layers must provide enough structure, so the insulating foams can only make up the middle layers. For the structural layers, the minimum thickness is driven by manufacturing constraints of the materials. Lastly, the total mass of the TPS cannot exceed 9 kg.

## 5.2 TPS Single Layer Implementation

The Crank-Nicolson finite difference method was used to numerically solve the one-dimensional heat equation for both the spatial and temporal temperature distribution in the TPS. The boundary condition at the front face of the TPS is that the heat conducted in equals the incident convective heating minus the radiated heat flux. At the back face, the heat conducted out must be the same as the radiated heat flux. The initial condition is that the temperature throughout the TPS starts at 343 K. The global density, global velocity, and adiabatic wall temperature are not coupled with the TPS parameters, so those quantities were used as calculated in Task 3 and interpolated at equal time steps throughout the trajectory. In contrast, the wall temperature and incident convective heating differ from Task 3, which assumed the adiabatic case, so those were recalculated at each time step in the numerical solution.

For the front face, the governing equation is

$$-T_1^{n+1} + T_2^{n+1} = -\frac{\Delta y}{\lambda_1}[q_1^C - \epsilon\sigma(T_1^n)^4] \tag{20}$$

where $\Delta y$ is the discretized TPS thickness, $\lambda_1$ is the thermal conductivity of the front face, $q_1^C$ is the incident convective heating, $\epsilon$ is the emissivity of the material, and $\sigma$ is the Stefan-Boltzmann constant. Note that $T_i^n$ is the temperature at time step n and node i within the TPS. Similarly, the back face is approximated as

$$-T_{N-1}^{n+1} + T_N^{n+1} = -\frac{\Delta y}{\lambda_N}\epsilon\sigma(T_N^n)^4 \tag{21}$$

where $\lambda_N$ is the thermal conductivity at the back face. The incident heating was calculated using the Tauber Menees relations for the stagnation point and the midpoint of the conical aeroshell, which was approximated as a flat plate at an angle from the flow. Note that the incident heating had to be recalculated at every time step since it is coupled with the wall temperature, or front face temperature.

For the inner layers, the Crank-Nicolson method yields

$$[-b_iT_{i-1} + (1 + b_i + b_{i+1})T_i - b_{i+1}T_{i+1}]^{n+1} = [b_iT_{i-1} + (1 - b_i - b_{i+1})T_i + b_{i+1}T_{i+1}]^n \tag{22}$$

In this equation $b_i = \frac{1}{2}\frac{\Delta t}{\Delta y^2}\alpha_{i+1/2}$, and $\alpha_{i+1/2}$ is the average of $\alpha_i$ and $\alpha_{i+1}$. Note that $\alpha$ is the thermal diffusivity, and $\alpha = \frac{\lambda}{\rho c}$. $\lambda$ is the thermal conductivity, $\rho$ is the density, and $c$ is the specific heat capacity, all of which are material-dependent properties. In some cases, $\lambda$ varies with temperature, but for this analysis, it was assumed to be a constant average value. At interfaces between different layers, the thermal properties were taken as an average of those of the two layers.

### 5.2.1 TPS at Stagnation Point: Single Layer of FW 12

To confirm the numerical solution was correct, we first analyzed the stagnation point thermal behavior with one layer of TPS, specifically the ceramic material FW 12. The stagnation heating was calculated using the Tauber Menees relations that were used in Task 3, specifically equations 16 and 17. Figures 30 and 31 show the temporal and spatial distribution of the temperature throughout 10cm of FW 12. In Figure 30, it is clear that the peak temperature is well below the maximum operating temperature, and the back face temperature stays within the 70°C limit. It can also be seen that the peak temperature occurs at later times as you move through the TPS, which matches the physical process of heat moving through the material.

The spatial distribution in Figure 31 shows the temperature throughout the TPS at given instants in time. Depending on the thermal properties and incident convective heating, there reaches a point where the maximum temperature shifts inside of the TPS instead of being at the front face. There are two drivers behind this, specifically that the incident heating decreases after the peak around 100 s and that the front face radiates heat outward. Additionally, this figure highlights that the last 3cm maintain
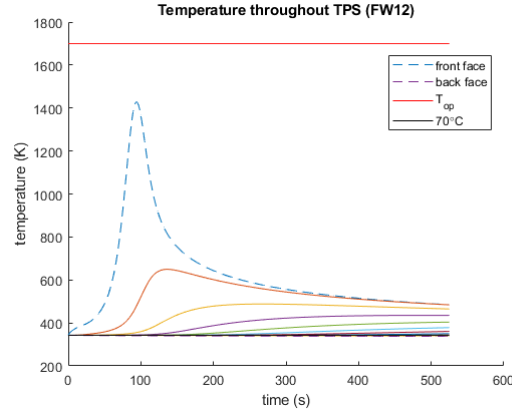
Figure 30: Temporal temperature distribution throughout 10cm of FW 12
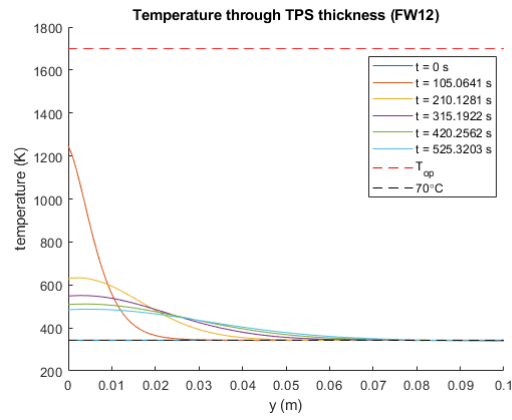


Figure 31: Spatial temperature distribution throughout 10cm of FW 12

a constant temperature throughout the flight path, indicating that lower thicknesses would meet the temperature requirements.

To further confirm the accuracy of the numerical solution, Figures 32 and 33 show the temporal and spatial temperature distributions for 5cm of FW 12. The 70°C requirement at the back face is not met since the back face temperature increases over time. Furthermore, the temperature throughout the TPS converges more rapidly than the 10cm case since the heat is conducted through the full thickness more quickly.
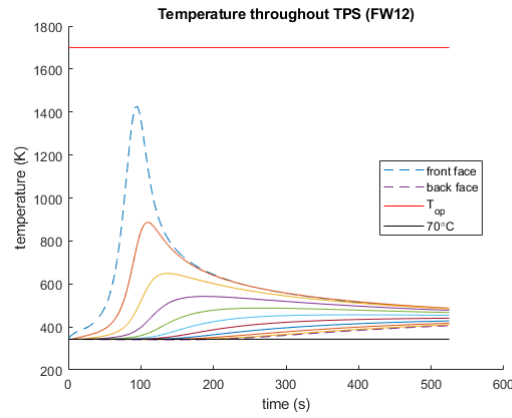


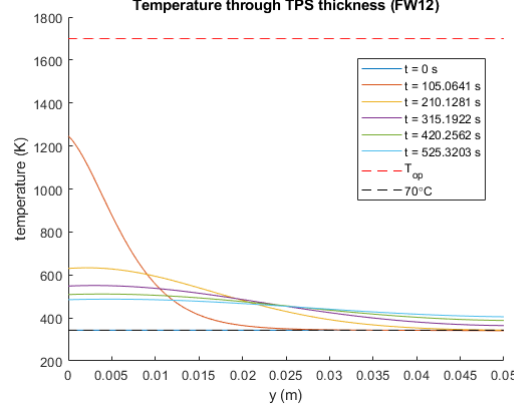Figure 32: Temporal temperature distribution throughout 5cm of FW 12

Figure 33: Spatial temperature distribution throughout 5cm of FW 12

### 5.2.2 TPS at Conical Midpoint: Single Layer of Nextel 312

The analysis for the conical section was very similar to that at the stagnation point, with a different Tauber Menees relation for the incident convective heating as shown in equations 16 and 19. Specifically, the conical section was modeled as a flat plat at an angle with respect to the incoming flow, and the adiabatic wall temperature was calculated using local flow conditions after an oblique shock. An important parameter is the curvilinear coordinate along the capsule, which was calculated with the stagnation point as the origin.

Overall, the trends for 2.5cm of Nextel 312 are similar to those of 10cm of FW 12. Specifically, the operating temperature and payload temperature requirements are both met, and the timing of the temperature peak shifts throughout the TPS, as shown in Figure 34. In Figure 35, the spatial peak temperature shift is once again evident, and the last 1cm stays within a narrow temperature range throughout the trajectory. Furthermore, it is clear that the back face temperature decreases over time, indicating that this TPS is handling the incoming heat load better than what is required.
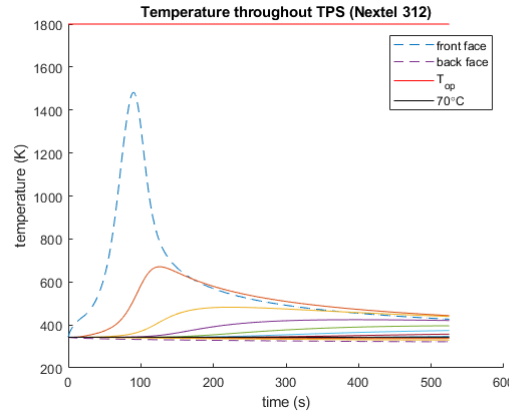


Figure 34: Temporal temperature distribution throughout 2.5cm of Nextel 312

A key point shown in Figures 34 and 35 is that the temperatures are very similar to those with 10cm of FW 12 at the stagnation point (Figures 30 and 31), despite having a quarter of the TPS thickness. Some differences are due to material properties, but the primary reason is that the incident convective heating is about half of that at the stagnation point, as shown in Figure 36. Thus, it is expected that the optimal TPS layering for the conical part will be thinner than that for the spherical nose cap.

To further validate the code for the conical part, Figures 37 and 38 show the temperature distributions at the conical midpoint with 1.25cm of Nextel 312. Similar to the stagnation point, the back face temperature requirement is not met, and the temperature within the TPS converges more quickly since there is less material.

These single layer approximations confirmed that the algorithm was working and provided accurate results that matched what is physically expected given the thermal loads throughout the trajectory. The
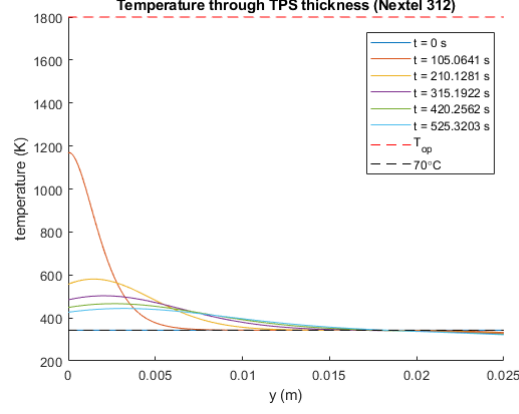
Figure 35: Spatial temperature distribution throughout 2.5cm of Nextel 312
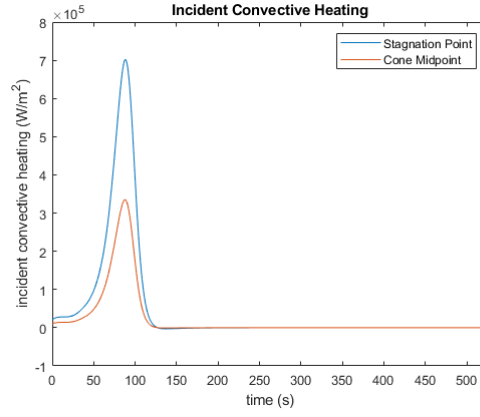


Figure 36: Incident convective heating coupled with TPS analysis for the stagnation point and mid-point of the conical section
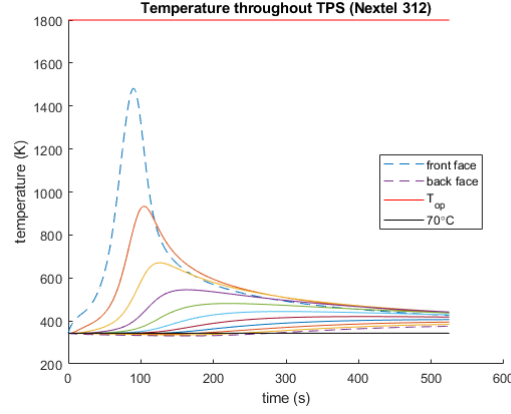


Figure 37: Temporal temperature distribution throughout 1.25cm of Nextel 312

final step was to modify the code to allow for multilayer TPS schemes and calculate the optimal layering strategies to meet both the temperature and mass requirements.

## 5.3 TPS Multilayer Optimization

When selecting materials to use for TPS layering, it is important to consider material properties and which layers act as a heat sink versus an insulator. For the outer layers, it is best to have a material with high thermal conductivity so that the heat is quickly distributed throughout the material, thereby preventing the front face from exceeding the maximum operating temperature. For the inner layers, it is
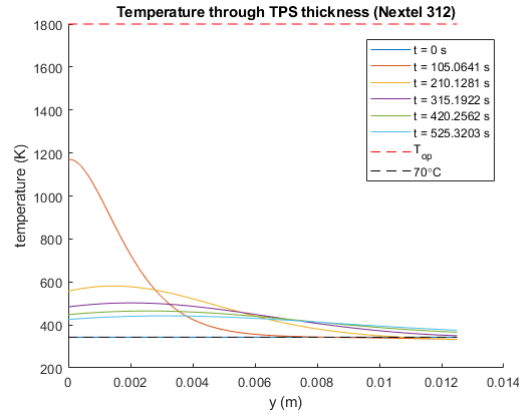
Figure 38: Spatial temperature distribution throughout 1.25cm of Nextel 312

better to use materials with low thermal conductivity that act as insulators and prevent the heat from reaching the back surface, and ultimately the payload. Lastly, the density of each material is important due to the mass constraints of the capsule.

In general, the incident heating rate informs the choice of material, and the total heat flux throughout the trajectory drives the required thickness.

### 5.3.1 Material Selection

For the TPS material selection, we look to use Commercial-off-the-shelf (COTS) products. This allows for a reduction of cost, reduced development time, and lower life cycle costs. The materials chosen for the rigid TPS and their properties are listed below in Figure 39.

| Material | Density [kg/m3] | Thermal Conductivity [W/mK] | Specific Heat [J/kgK] | Operational Temperature [C] | Emissivity |
|----------|-----------------|------------------------------|------------------------|------------------------------|------------|
| FW12 Ceramic | 2900 | 2.73 | 1050 | 1700 | 0.87 |
| RESCOR 310M | 800 | 0.187 | 1457 | 1650 | |
| INTEK-PFI-1120 FOAM | 6.4 | 0.046 | 1009 | 300 | |
| FW12 Ceramic | 2900 | 2.73 | 1050 | 1700 | 0.87 |

Figure 39: Table of parameters for materials chosen for rigid TPS by layer.

The first and fourth layers will be made of the FW12 ceramic, providing the stiffness we need for the TPS design. The internal layers use insulating material to slow down the thermal wave, as we want to keep the back wall temperature below 343 K.

The materials chosen for the flexible TPS are shown in Figure 40

xxiii

| Material | Density [kg/m3] | Thermal Conductivity [W/mK] | Specific Heat [J/kgK] | Operational Temperature [C] | Technological thickness [mm] | Emissivity |
|---|---|---|---|---|---|---|
| Nextel 312 | 2700 | 0.15 | 1047 | 1800 | 0.25 | 0.88 |
| Sigratherm | 800 | 0.055 | 700 | 1000 | 0.15 | |
| Pyrogel 6650 | 6.4 | 0.02 | 1150 | 650 | 5 | |
| Nextel 312 | 2700 | 0.15 | 1047 | 1800 | 0.25 | 0.88 |

Figure 40: Table of parameters for materials chosen for flexible TPS by layer.

Again, we choose the outer layers for structural support, and the inner layers must have adequate insulating properties to keep the back wall cool.

### 5.3.2 Multilayer Integration

Integrating the 1D heat equation in the multilayer case is quite similar to the single layer case, except we now have our material properties changing throughout the thickness. In order to model this property variation accurately, the material properties at material interfaces were defined to be an average of the two materials, to smoothen out the discontinuities in material properties.

Once we could integrate the 1D heat equation in the multilayer case, we inputted various "unoptimized TPS layouts."

Figure 41 shows the unoptimized multilayer TPS temperature history over the flight. The thicknesses in this case are 5mm for the first layer, 10mm for the second, 10mm for the third, and 5mm for the fourth.
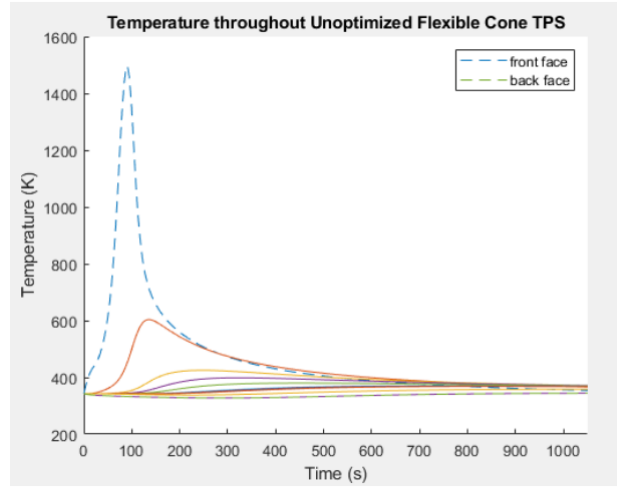


Figure 41: Temperature history for Unoptimized Flexible TPS.

We find that this TPS layout meets all of the maximum temperature requirements, but fails to meet the mass requirement, as it is 23.65 kg. We now develop an algorithm to find an optimal TPS layout.

### 5.3.3 Algorithm

The optimization of the Thermal Protection System (TPS) was done using the optimization algorithm depicted in Figure 42. We begin the algorithm with an initial candidate solution based on the unoptimized TPS analysis done previously. The corresponding back wall temperature is then calculated and corresponding steps are taken towards adjusting the TPS in order for it to meet the back wall temperature requirement. This updated candidate solution is then fed into the front wall temperature iterator where the thicknesses are once again adjusted until they meet the requirement. Once the candidate
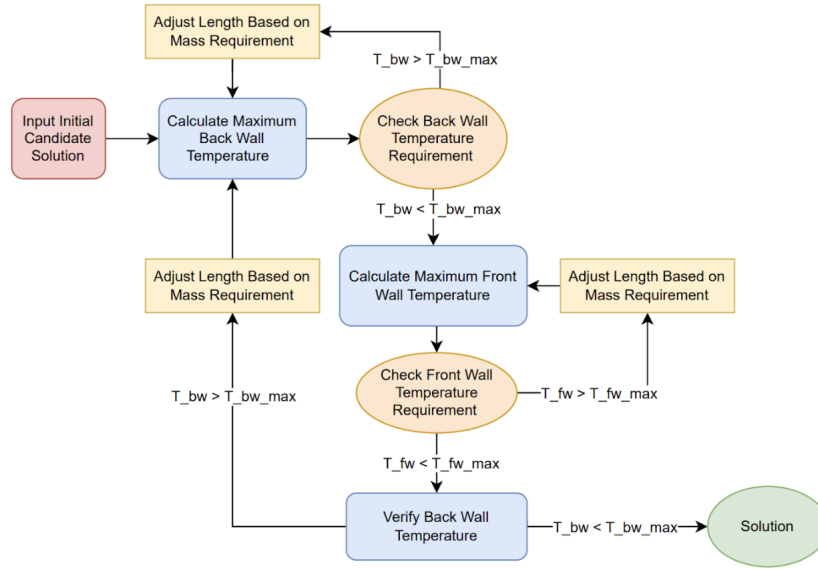
Figure 42: Optimization Algorithm

solution is updated accordingly it is once compared to the back wall temperature requirement. At this point in the algorithm, with both conditions met, our algorithm exports a solution. It is important to note that we have implemented the mass constraint implicitly, by making sure that we never exceed the mass requirement whenever the thicknesses are increased.

### 5.3.4 Solution

We found that the most restrictive requirement was the back face temperature limit. All of our solutions were well within the operational temperature limits, but each solution was right at the edge of our back face temperature requirement being met.

For the rigid nose TPS, our algorithm computes the layout as 3mm of FW12 Ceramic, followed by 40mm of RESCOR 310M, followed by 25mm of INTEK-PFI-1120 FOAM, and finally another 2mm of FW12 Ceramic. The temperature profiles are presented in Figure 43 and **??**.
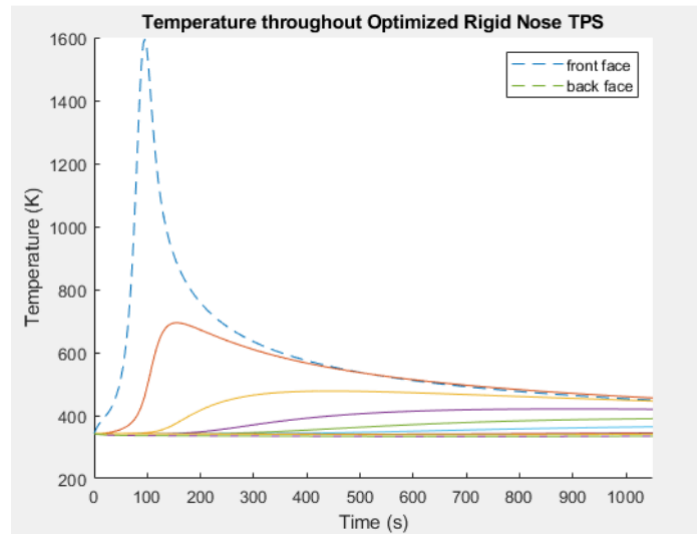


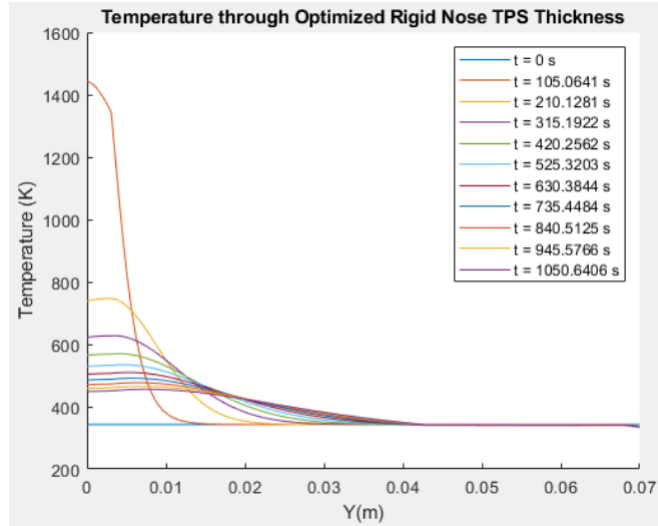Figure 43: Temperature profile for Optimized Rigid Nose TPS.

Figure 44: Temperature profile through thickness for Optimized Rigid Nose TPS.

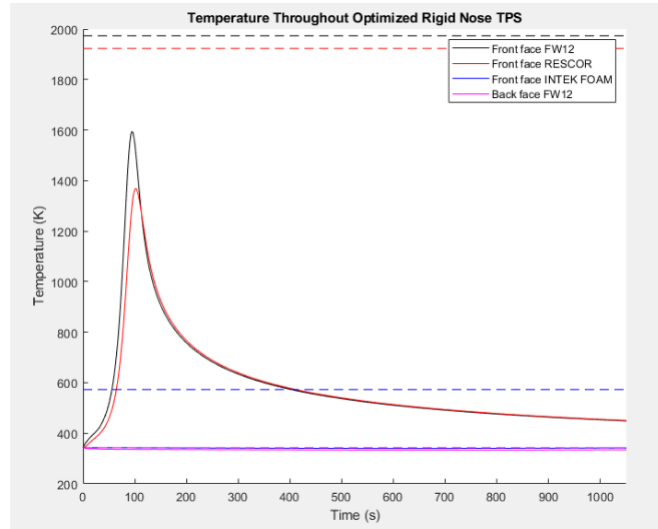We show that this solution meets all of the temperature requirements in Figure 45.



Figure 45: Temperature profiles for each material, dashed lines indicate $T_{op}$.

This solution gave us a mass of 2.095 kg. Moving on to the flexible TPS For the flexible cone TPS, our algorithm computes the layout as 0.25mm of Nextel 312, followed by 13mm of Sigratherm, followed by 30mm of Pyrogel 6650, and finally another 0.25mm of FW12 Ceramic. This gives a mass of 6.674 kg. The temperature profiles are presented in Figure 46 and 47.
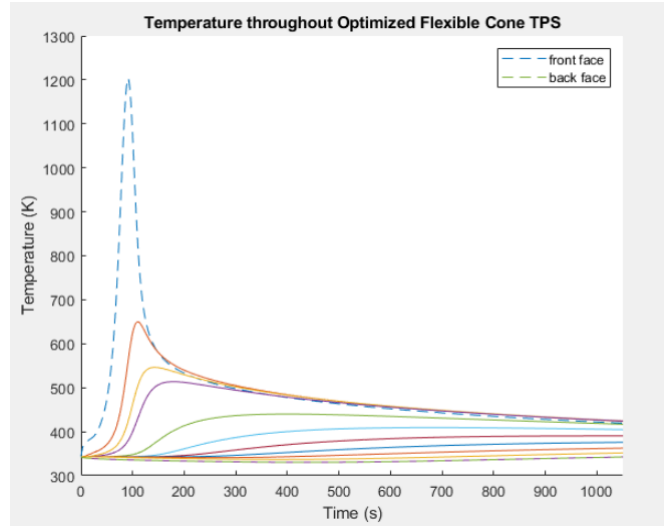
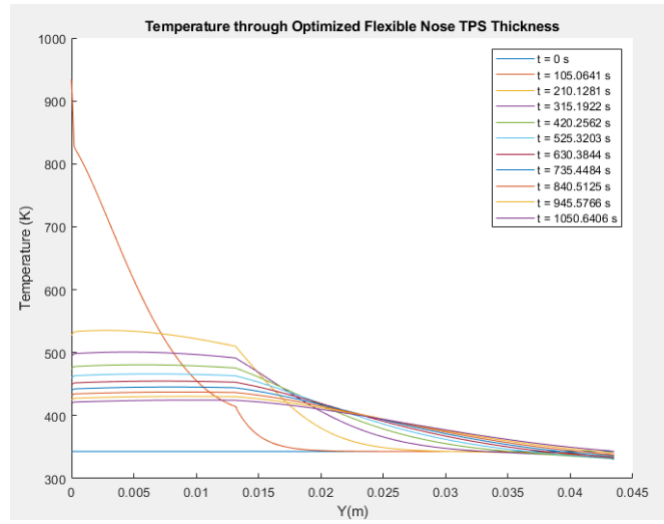Figure 46: Temperature profile for Optimized Flexible Cone TPS.



Figure 47: Temperature profile through thickness for Optimized Flexible Cone TPS.

As for the nose TPS, we show that this solution meets all of the temperature requirements in Figure 48.
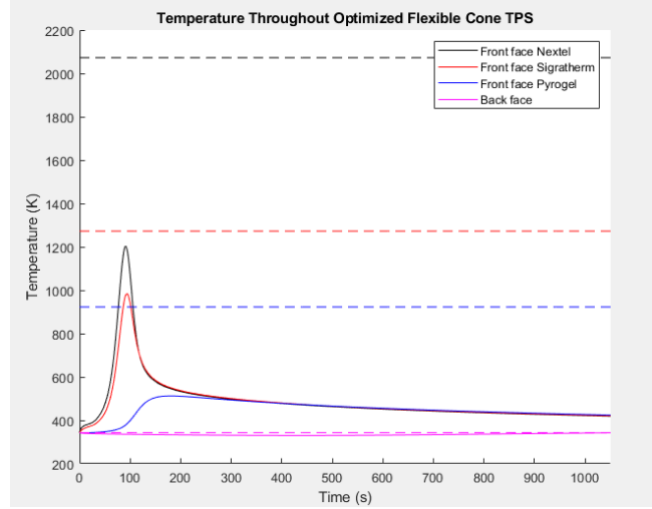
Figure 48: Temperature profiles for each material, dashed lines indicate $T_{op}$.

### 5.3.5 Final TPS Solution

The final solution for the thicknesses and materials of our TPS (found via the optimization algorithm) are shown in Tables 1 and 2 for both the Rigid and Flexible TPS.

| Rigid Thermal Protection System (TPS) Thicknesses for the Nose | |
|---|---|
| Layer 1 | 3 mm |
| Layer 2 | 40 mm |
| Layer 3 | 25 mm |
| Layer 4 | 2 mm |
| **Total** | 70 mm |

Table 1: Rigid Thermal Protection System (TPS) Thicknesses for the Nose

| Flexible Thermal Protection System (TPS) Thicknesses for the Cone | |
|---|---|
| Layer 1 | 0.25 mm |
| Layer 2 | 13 mm |
| Layer 3 | 30 mm |
| Layer 4 | 0.25 mm |
| **Total** | 43.5 mm |

Table 2: Flexible Thermal Protection System (TPS) Thicknesses for the Cone

| Mass of the Ballistic Re-Entry Vehicle TPS | |
|---|---|
| Rigid Nose TPS | 2.095 kg |
| Flexible Cone TPS | 6.674 kg |
| **Total** | 8.769 kg |

Table 3: Mass Distribution for TPS in the Nose and Cone of the Vehicle

These thicknesses correspond to the masses in Table 3. It is important to note that we had to loosen the constraint of the weight on the cone TPS alone since we could not find a solution that met both the mass and temperature requirements. As a result, we decided to exceed this subconstraint, so that we could find a solution that would at least meet the overall mass requirement on the total TPS added to the vehicle which is perhaps the most important in this application.

# 6  Conclusion

Throughout this project we explored the various steps involved in develeoping a holistic aerothermodynamic analysis of a ballistic re-entry vehicle for the purpose of designing an optimal Thermal Protection System. In the first phase of the project, we approximated the trajectory using assumptions on the ballistic coefficient, which provided some insight into the flight path as well as the velocities and dynamic pressures we would expect along the trajectory. In the second phase, we began using these conditions to develop an aerodynamic understanding of the vehicle via pressure coefficient, lift coefficient, drag coefficient, and moment coefficient analysis. After developing a corresponding look-up table with the results of this analysis for various Mach numbers and angles of attack, we recalculated an optimal trajectory for the vehicle. We then proceeded to Phase 3 where we used the new flight trajectory values to analyze the heat flux acting on the vehicle along the trajectory. We concluded the project with Phase 4 where we utilized the aerothermodynamic analyses to design an optimal thermal protection system (TPS) for the nose and cone sections of the vehicle. The results for this final solution of the TPS thicknesses and masses are shown in Tables 1, 2, and 3. Overall this project has given us a through understanding of the aerothermodynamic coupling that exists in hypersonic flow problems and the implications this has on the design from an aerodynamic and thermal point of view.